Article:

Blackburn, L.R., Sun, S.-K., Lawson, S.M. et al. (2020) Synthesis and characterisation of Ca1-xCexZrTi2-2xCr2xO7: Analogue zirconolite wasteform for the immobilisation of stockpiled UK plutonium. Journal of the European Ceramic Society, 40 (15). pp. 5909-5919. ISSN: 0955-2219

https://doi.org/10.1016/j.jeurceramsoc.2020.05.066

Journal of the European Ceramic Society xxx (xxxx) xxx–xxx

Contents lists available at ScienceDirect

Journal of the European Ceramic Society

journal homepage: www.elsevier.com/locate/jeurceramsoc

Original Article

Synthesis and characterisation of $Ca_{1-x}Ce_xZrTi_{2-2x}Cr_{2x}O_7$: Analogue zirconolite wasteform for the immobilisation of stockpiled UK plutonium

Lewis R. Blackburn[a], Shi-Kuan Sun[a,*], Sebastian M. Lawson[a], Laura J. Gardner[a], Hao Ding[a], Claire L. Corkhill[a], Ewan R. Maddrell[b], Martin C. Stennett[a], Neil C. Hyatt[a,*]

[a] Immobilisation Science Laboratory, University of Sheffield, Department of Materials Science and Engineering, Sir Robert Hadfield Building, Mappin Street, S1 3JD, UK
[b] National Nuclear Laboratory, Workington, Cumbria, CA14 3YQ, UK

ARTICLE INFO

Keywords:
Zirconolite
Immobilisation
Plutonium
Surrogate
Wasteform

ABSTRACT

A series of $Ca_{1-x}Ce_xZrTi_{2-2x}Cr_{2x}O_7$ zirconolite ceramics ($0 \leq x \leq 0.35$) were reactively sintered in air at 1350 °C for 20 h. Single phase zirconolite-2M was formed for $x \leq 0.15$, with Cr_2O_3 and an undesirable Ce-bearing perovskite phase present above $x = 0.20$. Electron diffraction analysis confirmed that the zirconolite-2M polytype was maintained over the solid solution. X-ray absorption near edge structure (XANES) data determined that between 10–20% Ce was speciated as Ce^{3+}, and Cr was present uniformly as Cr^{3+} with near edge features consistent with occupation of octahedral sites within the zirconolite-2M structure. A sample corresponding to $x = 0.20$ was processed by reactive spark plasma sintering (RSPS), with a rapid processing time of less than 1 h. XANES data confirmed complete reduction to Ce^{3+} during RSPS, promoting the formation of a Ce-bearing perovskite, comprising 19.3 ± 0.4 wt. % of the phase assemblage.

1. Introduction

The safe handling and conditioning of highly radioactive materials derived from nuclear fuel reprocessing operations is an issue of scientific and socioeconomic importance. In the United Kingdom, a large stockpile of separated civil plutonium oxide (PuO_2) has amassed from spent fuel reprocessing *via* the PUREX (Plutonium-Uranium-Reduction-Extraction) process [1]. This stockpile is forecast to peak at 140 teHM (tonnes of heavy metal equivalent), following cancellation of the Fast Neutron Reactor programme in 1994, which has led to the need for other Pu management strategies, for example reuse as mixed oxide (U, Pu)O_2 (MOX) fuel in light water reactors [2]. Currently, MOX fuel presents a commercially unattractive prospect in the UK. The Nuclear Decommissioning Authority (NDA, UK) have assessed it to be a credible option, although appetite for offtake from commercial operators is weak [2]. A fraction of the Pu stockpile has also been declared unsuitable for MOX fabrication, due to chlorine contamination arising from long term storage in polyvinyl chloride (PVC) packaging [3]. An alternative approach is the conditioning of the Pu stockpile and waste material *via* immobilisation within a ceramic matrix.

Immobilisation within ceramic matrices is considered a viable option for the conditioning of actinides such as Pu, since crystalline materials generally offer superior aqueous durability with respect to borosilicate glasses currently used for the vitrification of high level nuclear waste calcines [4–6]. Zirconolite is a naturally occurring titanate ceramic closely related to the pyrochlore family of minerals, with general structure $A_2B_2O_7$ [7]. Zirconolite has nominal stoichiometry $CaZr_xTi_{3-x}O_7$, and crystallises in the zirconolite-2M polytype for $0.85 \leq x \leq 1.30$, in space group C2/*c* [8]. This structure consists of ZrO_7 and CaO_8 polyhedra integrated between corner sharing TiO_6/TiO_5 polyhedra arranged in a hexagonal tungsten bronze-style motif. This two-layer repeat constitutes the zirconolite-2M unit cell [9]. Zirconolite can exhibit extensive polytypical behaviours which are characterised by the stacking sequence between CaO_8/ZrO_7 polyhedra and TiO_6 layers; the crystallisation of zirconolite polytypes occurs as a result of lanthanide/actinide incorporation and partial oxygen pressure. For example, the zirconolite-4M polytype was observed to form as an intermediate phase in $Ca_{1-x}Zr_{1-x}Nd_{2x}Ti_2O_7$ system and is described as an intercalated sequence of zirconolite-2M and pyrochlore type modules [10,11]. The flexibility of zirconolite and its respective polytypes to incorporate a wide variety of lanthanide and actinides within its structure makes it an ideal candidate for the disposition of excess Pu. The aim of this work is to evaluate the effectiveness of Cr^{3+} as a charge balancing species for the immobilisation of Ce; in this instance, Ce^{4+} is applied as a surrogate for Pu^{4+}. Cerium is justified as a suitable surrogate on the basis of safety and expediency, however, the variations with respect to redox

---

* Corresponding authors.
E-mail addresses: shikuan.sun@sheffield.ac.uk (S.-K. Sun), n.c.hyatt@sheffield.ac.uk (N.C. Hyatt).

https://doi.org/10.1016/j.jeurceramsoc.2020.05.066
Received 22 April 2020; Received in revised form 25 May 2020; Accepted 26 May 2020

Please cite this article as: Lewis R. Blackburn, et al., Journal of the European Ceramic Society, https://doi.org/10.1016/j.jeurceramsoc.2020.05.066

potential have been largely realised [12]. Compositions were fabricated by conventional solid state reaction – sintering of the compositional range $Ca_{1-x}Ce_xZrTi_{2-2x}Cr_{2x}O_7$ ($0.00 \leq x \leq 0.35$) and the phase evolution of zirconolite was characterised to determine the incorporation of Ce, using Cr^{3+} to maintain electro-neutrality across the target zirconolite phase. The solid solution parameter x was limited at x = 0.35 as this would correspond to an upper Pu content of ~ 20 wt. %, which is of interest for application. Reactive Spark Plasma Sintering (RSPS) [13] was successfully applied to produce $Ca_{0.80}Ce_{0.20}ZrTi_{1.60}Cr_{0.40}O_7$ (x = 0.20) ceramics of near theoretical density, however, this afforded complete reduction to Ce^{3+}, with a deleterious impact on the phase assemblage, as a result of the use of graphite die and vacuum in the SPS system [14].

2. Experimental

2.1. Materials synthesis

All compositions were synthesised by conventional solid state reaction – sintering between $CaTiO_3$ (Sigma Aldrich, 99.9 % trace metals basis), ZrO_2 (Sigma Aldrich, 99.9 % trace metals basis), Cr_2O_3 (Sigma Aldrich, 99.9 % trace metals basis), TiO_2 (anatase, Sigma Aldrich, 99.9 % trace metals basis) and CeO_2 (Acros Organics, 99.9 % trace metals basis). Precursor materials were dried and weighed according to $Ca_{1-x}Ce_xZrTi_{2-2x}Cr_{2x}O_7$ where $0.00 \leq x \leq 0.35$ ($\Delta x = 0.05$ increments). Batches were homogenised by planetary milling at 400 rpm for 20 min, using isopropanol as a milling agent. Slurries were discharged and left for 12 h at 90 °C to evaporate excess solvent. Approximately 0.3 g of dried material was uniaxially pressed into 10 mm green body pellets under a force of 3 t (~ 260 MPa), and reacted for 20 h in air at 1350 °C. A specimen was also produced by reactive spark plasma sintering (RSPS). Powder mixture with nominal composition $Ca_{0.80}Ce_{0.20}ZrTi_{1.60}Cr_{0.40}O_7$ (x = 0.20) was pressed into a graphite die (with graphite foil spacers) then sintered using a HP-D 1050 SPS system at 1320 °C under vacuum with a dwell time of 30 min (100 °C/min, 5 V and 1 kA at maximum sintering temperature). During the sintering process, the uniaxial pressure was maintained at 15 MPa.

2.2. Materials characterisation

Samples were prepared for powder X-ray diffraction (XRD) by hand grinding the reacted specimens in an agate pestle and mortar using IPA. A Bruker D2 Phaser diffractometer fitted with Lynxeye position sensitive detector was used; diffraction data were acquired in the range $5^\circ \leq 2\theta \leq 80^\circ$, with step size of 0.02° and 1 s per step, using Cu Kα radiation ($\lambda = 1.5418$ Å, Ni filter). Unit cell parameters for the zirconolite unit cell and quantitative phase analysis (QPA) were calculated using the Rietveld method, using the GSAS software with EXPGUI interface [15]. Samples were sectioned, mounted in cold setting resin, and polished to a 1 μm optical finish with diamond suspension prior to microstructure analysis using a Hitachi TM3030 scanning electron microscope (SEM), operating with a 15 kV accelerating voltage and a working distance of approximately 8 mm. Energy dispersive X-ray spectroscopy (EDS) was undertaken using a Bruker Quantax Energy Dispersive X-ray Spectrometer for compositional analysis.

Ce L_3 XANES and Cr K XANES (X-ray absorption near edge structure) spectra for cold pressed and sintered samples (CPS) were acquired on beamline B18 at the Diamond Light Source (Oxford, UK) which operates at 3 GeV with a ring current of 300 mA. B18 is a bending magnet beamline producing X-rays in the energy range 2–20 keV. The optical arrangement consists of a water cooled vertically collimated Si mirror, a double crystal Si(111) monochromator, a double toroidal focusing mirror, and harmonic rejection mirrors. Samples were measured in QuEXAFS mode with simultaneous collection of transmission and fluorescence data. Cr K-edge spectra were recorded between 5789 and 6550 eV in energy steps of 0.2 eV using an acquisition time of 35 ms $step^{-1}$. Ce L_3-edge spectra were recorded between 5523 and 6154 eV in energy steps of 0.25 eV using an acquisition time of 50 ms $step^{-1}$. To improve data quality, the beam spot size was defocused to *ca.* 1.0 mm and multiple scans were acquired and averaged. Incident and transmitted beam intensities were measured using ionisation chambers which were filled with mixtures of He and N_2 gas. Fluorescence emission was detected using a 36 channel Ge solid state detector. In order to ensure energy reproducibility (± 0.05 eV) and allow absolute energy calibration, a Cr foil was measured in the reference measurement position; the edge position (measured as the first inflection point in the derivative of the absorption) was aligned to the expected value of 5989 eV [16].

XANES data for the sample processed by RSPS was acquired at the Ce L_3-edge on beamline BL-27B at the Photon Factory (PF) accelerator-based light source facility (Tsukuba, Japan). The PF operates at 2.5 GeV with a ring current of 300 mA, and supplies beamline BL-27B with radiation energy in the energy range 4–20 keV *via* a bending magnet. The optical arrangement consists of a double crystal Si(111) monochromator and slits were used to reduce the size of the beam to 3 mm in the horizontal and 1 mm in the vertical. The incident and transmitted photon spectra were measured with ionisation chambers which were gas filled to absorb *ca.* 20 % of the X-rays in the front chamber and 90 % in the second chamber [17]. Spectra were recorded between 5590 and 5990 eV with energy steps of 5 eV (5590–5690), 0.5 eV (5690–5790), 1 eV (5790–5890) and 5 eV (5890–5990). An accumulation time of 1 s $step^{-1}$ was used for all regions and multiple scans were acquired and averaged to improve the signal to noise. To ensure energy reproducibility (± 0.05 eV) a spectrum was collected from a $CePO_4$ standard between each sample.

Specimens were prepared for measurement by homogenising and suspended in polyethylene glycol (PEG) to produce samples with a thickness of approximately one absorption length. Spectra were also acquired from a selection of standards: CeO_2, $CePO_4$, $KCrO_3$, Cr_2O_3 and CrO_2. Data reduction and analysis was performed using the Demeter software package [18]. A linear combination fit of Ce L_3-edge XANES spectra was performed with respect to standards, in order to determine the relative amount of $Ce^{3+/4+}$ species. The corresponding R-factor (mean square sum of the residual for each data point) was determined. The pre-edge region in the Cr XANES spectra were deconvoluted by an edge step (modelled by an arctangent function) and three pre-edge features (fitted by Gaussian functions). To ensure fitting quality, the R-factor was optimised below 0.001. This methodology was based on the work of Wilke et al. [19].

Raman spectra of powdered specimens were collected using the Horiba-XploRA Plus system with 532 nm air cooled Ar^+ laser line and laser power of approximately 5 mW. Specimens for transmission electron microscopy were prepared *via* the powder route. Powders derived from the grinding of the sintered pellets were dispersed with isopropanol, with a small amount of the mixture pipetted from the top of the solvent line onto a holey lined Cu grid (Agar). Selected Area Electron Diffraction patterns (SAED) were acquired for specimens with nominal composition x = 0.05 and x = 0.35, using an FEI Tecnai T20 operating at 200 keV. SAEDPs were captured using a CCD camera.

3. Results and discussion

3.1. Phase assemblage

It was determined from powder X-ray diffraction data (Fig. 1) that zirconolite-2M crystallised as the major phase for each composition in the range $0 \leq x \leq 0.35$ (space group $C2/c$, Z = 8). The Bragg position of theoretical zirconolite-2M reflections (ICSD – 190015) are in excellent agreement with experimental data. In Fig. 1, prominent reflections for the 2M phase are indexed with appropriate *(hkl)* indices. Secondary phases $CaTiO_3$ (perovskite) and Cr_2O_3 are highlighted by open and closed circles, respectively. When targeting nominal

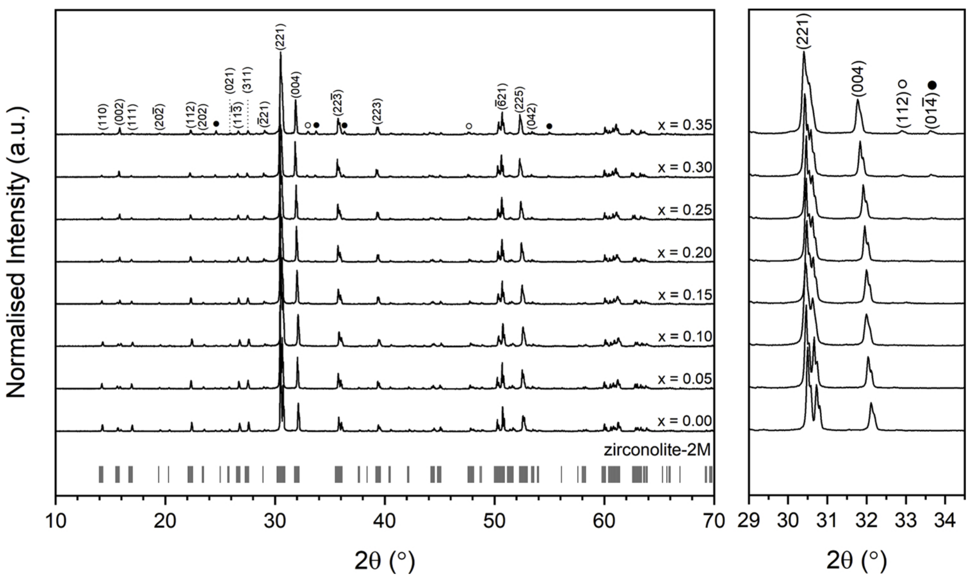

Fig. 1. Powder X-ray diffraction data of $Ca_{1-x}Ce_xZrTi_{2-2x}Cr_{2x}O_7$ ($0.00 \leq x \leq 0.35$) compositions synthesised at 1350 °C for 20 h in air. $CaTiO_3$ reflections are labelled by open circles; Cr_2O_3 reflections are labelled by black filled circles; vertical marks indicate Bragg positions of $CaZrTi_2O_7$ (ICSD – 190015).

$CaZrTi_2O_7$, single phase zirconolite adopting the 2M polytype was formed; unit cell parameters for x = 0.00 were derived from Rietveld fitting (Fig. 2) of XRD data: $\boldsymbol{a}$ = 12.4435(4) Å, $\boldsymbol{b}$ = 7.2735(3) Å, $\boldsymbol{c}$ = 11.3748(4) Å, $\boldsymbol{\beta}$ = 100.563(3)° and $\boldsymbol{V}$ = 1012.06(4) Å^3. These are in good agreement with previous reports [20]. The unit cell parameters for the zirconolite phase over the range $0 \leq x \leq 0.35$ are listed in Table 1. Zirconolite-2M was formed as a single phase in the compositional range $0 \leq x \leq 0.15$, indicating substitution of Ce and Cr into the host phase was achieved. However, minor reflections at $2\theta = 33.1°$ and $2\theta = 33.7°$ were evidenced for x = 0.20, which were attributed to $CaTiO_3$ and Cr_2O_3, comprising 1.2 ± 0.2 wt. % and 0.6 ± 0.2 wt. % of the total phase assemblage, respectively, as determined from the Rietveld analysis. With increased Ce/Cr content, $0.20 \leq x \leq 0.35$, greater relative proportions of $CaTiO_3$ and Cr_2O_3 secondary phases were found to be present, indicating the Ce and Cr were not fully substituted within the zirconolite-2M structure above x = 0.15. Despite the minor phase separation, zirconolite-2M remained present at approximately 94 wt. % when targeting x = 0.35, with perovskite accounting for ~ 3 wt. % of the total phase assemblage. Refinement of the powder diffraction data for the specimen corresponding to $x = 0.35$ is also displayed in Fig. 2.

Selected area electron diffraction (SAED) patterns for the $Ca_{0.95}Ce_{0.05}ZrTi_{1.90}Cr_{0.10}O_7$ (x = 0.05) and $Ca_{0.65}Ce_{0.35}ZrTi_{1,30}Cr_{0.70}O_7$ (x = 0.35) compositions are presented down the [010] direction in Fig. 3**a** and **b** and down the [111] direction in Fig. 3**c** and **d**, respectively. In both instances, the patterns indexed to the zirconolite-2M polytype (space group C2/*c*), in agreement with XRD data. There was no indication of polymorphic transitions to the zirconolite-4M or other polytypes, which has been previously observed when partitioning Ce/U in the Zr^{4+} site. For example, in the case of Vance et al., extensive "streaking" of crystalline reflections was observed in diffraction data for compositions of zirconolite-4M in the range $CaZr_{1-x}U_xTi_2O_7$ ($0.20 \leq x \leq 0.30$) [21].

3.2. Microstructure analysis

Polished surfaces for each composition were analysed by SEM-EDS analysis. A representative micrograph for x = 0.05 is displayed in Fig. 4. A matrix with homogeneous BSE contrast was observed, confirming the formation of single phase zirconolite-2M, with an average composition of $Ca_{1.01(7)}Ce_{0.03(1)}Zr_{0.88(9)}Ti_{2.00(5)}Cr_{0.08(1)}O_7$ determined by EDS analysis (oxygen content was assumed to be stoichiometric, given the poor sensitivity of EDS towards oxygen determination). The compositional analysis was in good agreement with targeted stoichiometry, considering the associated error of EDS analysis (quoted in parentheses to 1 s.d.). It was observed that all specimens exhibited a sintered microstructure but with high internal porosity; Archimedes density measurements and EDS data for each composition are summarised in Table 2. The high internal porosity would be undesirable from a disposability perspective, if replicated in a corresponding Pu solid solution. The porosity would result in an increased contact surface area available for dissolution, and this may be reduced by increasing the sintering temperature and/or applying the external pressure. It should be noted that with reference to the prototypical $CaZr_xTi_{3-x}O_7$ composition, the site occupancy and distribution of [Ti]/[Zr] is known to be sensitive to processing temperature: ratios between 1.31 and 2.75 at 1500 °C and 1300 °C have been reported, respectively [8]. Considering the processing temperature used (1350 °C), the observed [Ti]/[Zr] ratio falls within the expected range of values, considering the associated error of EDS analysis (quoted in parenthesis to 1 s.d.).

In agreement with powder XRD, no other phases were observed in the microstructure for x = 0.10 and x = 0.15 compositions (data not shown). Phase separation was observed in the microstructure at x = 0.20, shown in Fig. 5. Cr_2O_3 and perovskite were distinguished from the bulk matrix by BSE contrast. EDS analysis confirmed that Ce and Cr were also incorporated within the perovskite phase. The accommodation of Ce within the perovskite phase suggests partial Ce reduction to Ce^{3+}, as the formation of Ce^{3+} is known to promote and stabilise Ce-bearing perovskite [22,23]. A comparison of the EDS spectra of the perovskite phase and zirconolite-2M in the x = 0.35 composition is given in Fig. 6. Begg et al. reported that Ce^{3+} substituted within the Ca site in perovskite up to 0.1 f.u. without the need for charge balancing species [24]. However, in this instance, Cr^{3+} may provide sufficient charge compensation such that more Ce^{3+} can be incorporated within the perovskite phase. Indeed, $Ca_{0.9}Pu_{0.1}Ti_{0.8}Al_{0.2}O_3$ perovskite has been previously synthesised, hence the formation of Ce and Cr substituted counterparts is considered plausible, considering the similar electronegativity and size constraints for Ce/Pu and Cr/Al [25]. The microstructure for $0.25 \leq x \leq 0.35$ compositions displayed further phase separation, with Cr_2O_3 comprising 1.1 ± 0.2, 1.9 ± 0.2 and 2.5 ± 0.3 wt. % of the total phase assemblage, respectively. The zirconolite-2M phase fraction remained high, corresponding to 97.4 ± 0.02, 96.3 ± 0.03 and 93.5 ± 0.05 wt. % for x = 0.25, 0.30 and 0.35, respectively. A representative microstructure for the x = 0.35 sample, and elemental distributions, are

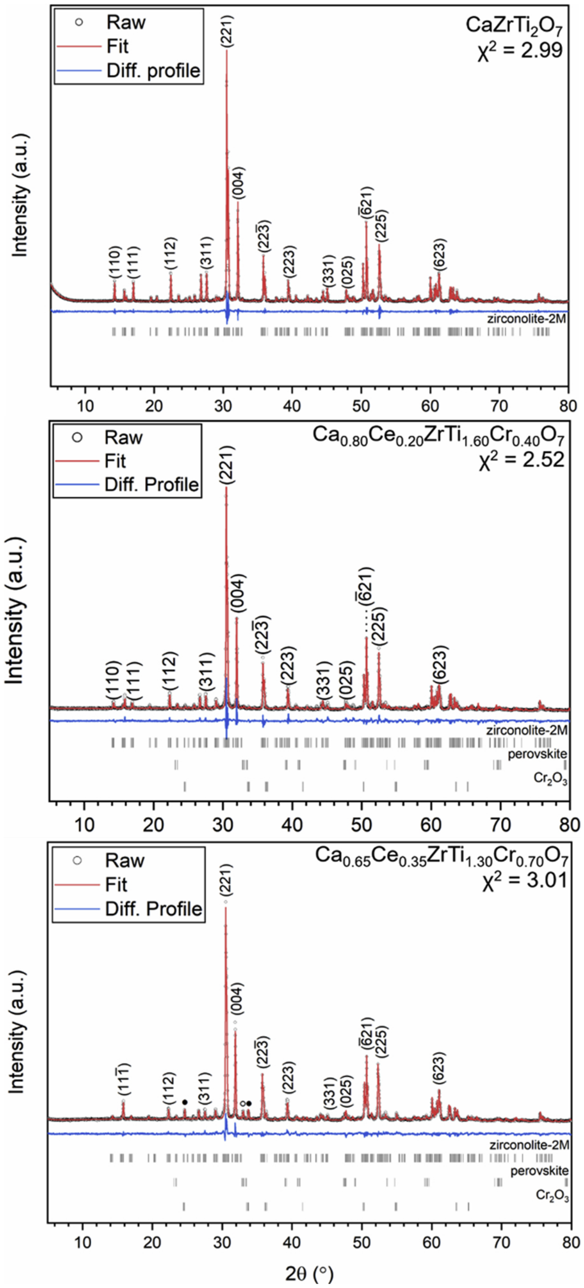

Fig. 2. Rietveld profile fit x = 0.00, x = 0.20 and x = 0.35. Recorded data is displayed in black; fit data is displayed in red; difference profile is displayed in blue. CaTiO$_3$ reflections are labelled by open circles; Cr$_2$O$_3$ reflections are labelled by black filled circles. Vertical marks indicate Bragg positions of CaZrTi$_2$O$_7$ (ICSD – 190015), CaTiO$_3$ (ICSD – 183209) and Cr$_2$O$_3$ (ICSD – 167268). (For interpretation of the references to colour in this figure legend, the reader is referred to the web version of this article).

displayed in Fig. 7. A minor fraction of unincorporated CeO$_2$ was evidenced in the x = 0.35 specimen by SEM analysis of the microstructure, yet, this was not detected by XRD. A ZrO$_2$ phase was also detected, however this constituted < 1 wt. % of the overall phase assemblage.

3.3. Oxidation state and local environment of Ce and Cr

Ce has been observed to exist as Ce^{4+} and Ce^{3+} in zirconolite wasteforms despite processing under oxidizing conditions. The oxidation state of cerium was determined through the use Ce L$_3$ XANES, acquired alongside Ce^{3+} and Ce^{4+} reference compounds (CePO$_4$ and CeO$_2$, respectively). These data are displayed in Fig. 8. The CePO$_4$ (monazite) spectrum was comprised of a single intense white line feature characteristic of Ce^{3+} speciation (in CePO$_4$ (monazite), Ce^{3+} is coordinated as a CeO$_9$ polyhedron). The white line features for CeO$_2$ consisted of an asymmetric doublet with lower relative intensity than observed for CePO$_4$ (in CeO$_2$, Ce^{4+} is coordinated as a CeO$_8$ polyhedron). The initial and final state electron configurations associated with the white line features for both reference compounds are discussed elsewhere [26]. It was apparent from visual inspection of normalised XANES spectra that Ce was present mainly as Ce^{4+} in Ca$_{1-x}$Ce$_x$ZrTi$_{2-2x}$Cr$_{2x}$O$_7$ compositions, remaining analogous to Pu^{4+}. However closer inspection of XANES data revealed a small shift in the edge position toward lower energy (with respect to the CeO$_2$ reference compound) and a small change in the relative intensity of the asymmetric doublet features, consistent with a minor fraction of Ce^{3+}. Linear combination fitting (LCF) of each composition was performed using the CeO$_2$ and CePO$_4$ reference compounds, the results are summarised in Table 3, which confirmed the presence of 15–30% Ce^{3+} depending on the composition. Reduction of Ce^{4+} to Ce^{3+} results in an increase in average ionic radius (0.97 Å–1.143 Å for 8-fold coordinated species [27]), favoring partitioning within the Ca^{2+} site in the perovskite phase, as was confirmed by SEM/EDS data.

XANES analysis at the Cr K-edge was undertaken on all compositions, and a series of Cr reference compounds representing various oxidation states and coordination environments. XANES spectra acquired at the Cr K-edge are displayed in Fig. 9. It was evident that all Cr-zirconolite specimens retained very similar edge features, consisting of an intense white line at approximately E$_0$ = 6002 eV (E$_0$ derived from the maxima of the first derivative). For all zirconolite spectra a minor pre-edge feature was also observed. The E$_0$ position of the Cr$_2$O$_3$ XANES spectrum was lower at approximately E$_0$ = 6000 eV, and the Cr$_2$O$_3$ white line also featured a significant shoulder on the absorption edge and a moderately intense pre-edge feature, which were not observed in the measured zirconolite spectra. The E$_0$ position and white line features for YCrO$_3$ were more consistent with features observed in the zirconolite XANES data, inferring similar Cr speciation and chemical environment. It was evident, therefore, that Cr was present primarily in a single dominant Cr environment, for all zirconolite compositions similar to that in YCrO$_3$, in which Cr^{3+} adopts octahedra coordination by oxygen. Furthermore, the XANES spectrum for K$_2$CrO$_4$ (in which Cr^{6+} adopts tetrahedral coordination by oxygen) is characterised by an intense pre-edge feature, which exists at ~ 15 eV prior to the main absorption edge. This feature was not observed for any Cr-containing zirconolite specimens, confirming the absence of Cr^{6+}. Several isosbestic points were also revealed as the concentration of *x* was increased – these are labelled as **A**, **B**, **C** and **D** on Fig. 9. The presence of isosbestic points in a closed system is attributed to the contribution of the absorbing atom (*i.e.* Cr) in two or more chemical environments. Considering the reference spectra for Cr$_2$O$_3$, the formation of isosbestic points is a result of increased contribution of free Cr$_2$O$_3$ present in the sample. Upon closer inspection, points **A**, **B**, **C** and **D** become apparent at some nominal composition in the interval 0.15 ≤ x ≤ 0.20. This was clearly distinguished by the appearance of the feature at 6012 eV (between points **B** and **C** in Fig. 9) which was common to both Cr$_2$O$_3$ and zirconolite spectra. The intensity of this feature increased with elevated Cr content, x > 0.15, suggesting the presence of Cr$_2$O$_3$. This is in agreement with powder XRD data and microscopic analysis, in which a secondary Cr$_2$O$_3$ phase was observed in the microstructure for compositions where x > 0.15. The pre-edge features in the XANES of Cr$_2$O$_3$, YCrO$_3$ and the x = 0.15 sample were deconvoluted by subtraction of a modelled arctangent function, and the features fitted by Gaussian functions. Considering Fig. 10, there are three distinct contributions to the Cr^{3+} pre-edge features in each instance. There were clear similarities between the features for the zirconolite pre-edge and YCrO$_3$ standard. The origin of the doublet feature for Cr^{3+} compounds in the pre-edge region are from quadrupolar 1 s → 3d transitions, as a result of

Table 1
Zirconolite-2M unit cell parameters for $Ca_{1\text{-}x}Ce_xZrTi_{2\text{-}2x}Cr_{2x}O_7$ (0.00 ≤ x ≤ 0.35) derived from Rietveld refinement fitting of powder X-ray diffraction data. Statistical errors are quoted in parentheses to 1 s.d.

Composition	Zirconolite-2M Unit Cell Parameters					
	a (Å)	*b* (Å)	*c* (Å)	*β* (°)	*V* (Å^3)	R_p (%), R_{wp} (%), χ^2
x = 0.00	12.4435(4)	7.2735(3)	11.3748(4)	100.563(3)	1012.06(4)	8.17, 6.28, 2.99
x = 0.05	12.4441(2)	7.2635(2)	11.3742(3)	100.580(3)	1010.62(3)	7.31, 5.75, 2.09
x = 0.10	12.4483(4)	7.2581(2)	11.3819(4)	100.582(3)	1010.88(4)	6.70, 5.15, 2.04
x = 0.15	12.4459(4)	7.2508(2)	11.3834(4)	100.582(3)	1009.79(4)	7.25, 5.65, 2.32
x = 0.20	12.4540(3)	7.2530(2)	11.3993(3)	100.569(3)	1012.23(4)	7.18, 5.54, 2.52
x = 0.25	12.4628(3)	7.2566(2)	11.4195(3)	100.548(3)	1015.31(4)	7.14, 5.47, 2.41
x = 0.30	12.4629(4)	7.2548(2)	11.4368(3)	100.518(3)	1016.69(4)	7.41, 5.70, 2.61
x = 0.35	12.4693(5)	7.2560(3)	11.4532(5)	100.500(3)	1018.89(5)	7.56, 5.74, 3.01

hybridisation of Cr-3d energy levels [28]. These data are in agreement with Cabaret et al. in which three local electric quadrupole transitions were predicted for K pre-edge features of octahedrally coordinated Cr^{3+} species from first principles [29]. The normalised intensity and energy centroid of the fitted Gaussian contributions to the pre-edge features of the x = 0.15 sample and $YCrO_3$ were determined to be similar. In the ideal $YCrO_3$ structure, CrO_6 octahedtra are arranged in a corner sharing motif, analogous to the hexagonal tungsten bronze layers of TiO_6 octahedra in the zirconolite structure. Cr_2O_3 also contains Cr^{3+} in octahedral coordination, however, the face and edge sharing of CrO_6 octahedra results in fitted Gaussian contributions to the pre-edge feature that are dissimilar in normalised intensity and centroid energy, compared to those of the x = 0.15 and $YCrO_3$. Thus, the Cr K-edge XANES analysis presented here is consistent with Cr substitution within the octahedral TiO_6 sites of the zirconolite structure.

Raman spectra in the wavenumber range 100 – 1000 cm^{-1} are presented in Fig. 11. Many active Raman vibrational modes are observed due to the low symmetry of the monoclinic unit cell. A prominent Raman mode at 780 cm^{-1} was observed for all samples, and a variety of intense modes were evidenced in the 150 – 400 cm^{-1} range.

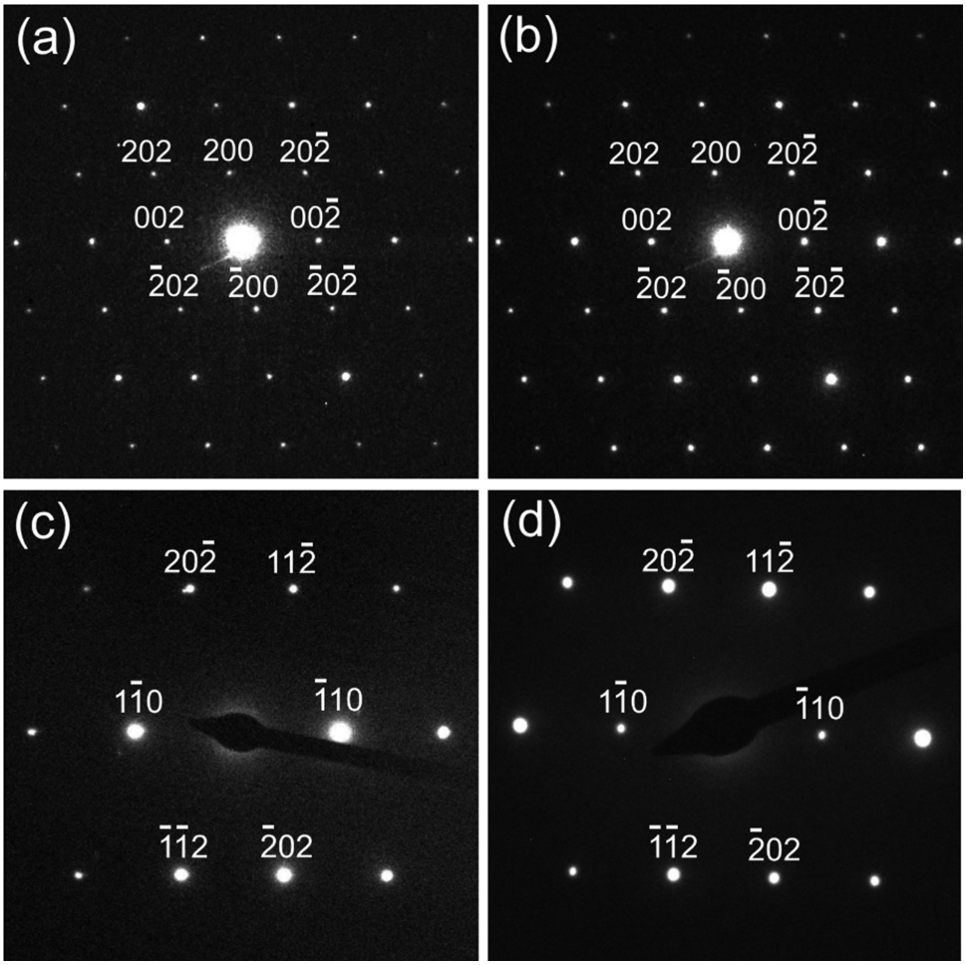

Fig. 3. Selected area electron diffraction patterns for (a) $Ca_{0.95}Ce_{0.05}ZrTi_{1.90}Cr_{0.10}O_7$; [010], (b) $Ca_{0.65}Ce_{0.35}ZrTi_{1.30}Cr_{0.70}O_7$; [010], (c) $Ca_{0.95}Ce_{0.05}ZrTi_{1.90}Cr_{0.10}O_7$; [111] and (d) $Ca_{0.65}Ce_{0.35}ZrTi_{1.30}Cr_{0.70}O_7$; [111].

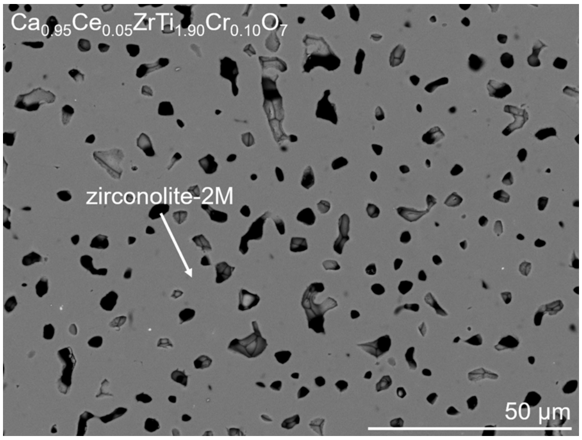

Fig. 4. Representative backscattered electron micrograph for specimen with nominal composition x = 0.05. Black regions are porosity.

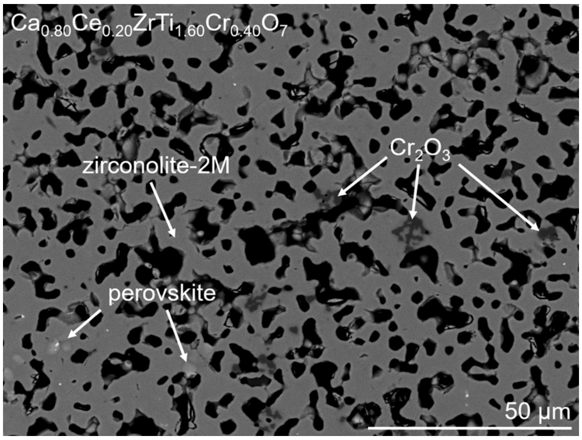

Fig. 5. Representative backscattered electron micrograph for specimen with nominal composition $Ca_{0.80}Ce_{0.20}ZrTi_{1.60}Cr_{0.40}O_7$ shows a mixture of zirconolite-2M, with minor $CaTiO_3$ and Cr_2O_3. Black regions are porosity.

At low concentrations *e.g.* x = 0.05, the spectrum is in good agreement with the active Raman modes observed in our previous studies for the zirconolite-2M structure [30]. As the substituted concentration is elevated, many of these features undergo broadening, in particular those at a lower Raman shift. This is attributed to disorder induced by Cr^{3+} and $Ce^{4+/3+}$ partitioning in Ti^{4+} and Ca^{2+} sites respectively. The degree of broadening does not appear to change beyond $x \geq 0.20$, consistent with the observations that Cr^{3+} was not fully incorporated into the zirconolite-2M structure beyond this concentration. Whilst it is known that the dominant vibrational mode at 780 cm^{-1} is attributed to the symmetric vibrations of TiO_6 octahedra, we are not aware of any studies that have directly assigned other prominent modes to specific bonds in the zirconolite structure [31]. However, it is generally accepted that vibrational modes below 700 cm^{-1} are attributed to CaO_8 and ZrO_7 polyhedral vibrations, and TiO_6 bending and stretching vibrations [30]. Jafar et al. performed Raman spectroscopic studies on the $CaZrTi_2O_7$ – $Y_2Ti_2O_7$ system, where a structural transition from zirconolite-2M to cubic pyrochlore was observed, with the formation of the zirconolite-4M polytype as an intermediate phase [32]. A characteristic feature of the transition to the zirconolite-4M and pyrochlore structures was the abatement of the TiO_6 peak at 780 cm^{-1}. This feature remains prominent in this instance, inferring zirconolite crystallised in the 2M configuration throughout the solid solution.

3.4. Reactive spark plasma sintering

In order to overcome poor densification observed in reactively sintered specimens, a sample of milled precursor with nominal composition x = 0.20 was processed by reactive spark plasma sintering (RSPS). It should be noted that this is not the same as *consolidation via* SPS, as in this instance, the reaction and consolidation occur simultaneously. Rather, here, we report the formation of heavily-doped zirconolite with a rapid processing time of less than 60 min. We have previously reported the formation of nearly single phase $CaZrTi_2O_7$ using this technique [13]. Whilst zirconolite wasteforms with incorporated Ce were reported by Clark et al., these were only consolidated by SPS subsequent to zirconolite formation *via* solid state reaction [22,33]. Powder XRD data comparing the phase assemblage of the RSPS and CPS product are displayed in Fig. 12. The sample processed by RSPS formed zirconolite-2M as the major phase, comprising 64.9 ± 0.2 wt. % of the overall phase assemblage. It was noted that relative phase fraction of perovskite (labelled with closed circles on Fig. 12) significantly increased in comparison to the CPS sample, from 1.2 ± 0.2 wt. % to 19.3 ± 0.4 wt % of the phase assemblage. There was also an increase in the quantity of ZrO_2 (labelled by open circles on Fig. 12), however this was still < 3 wt. % of the overall phase assemblage. A relative increase in Cr_2O_3 was also observed, from 0.6 ± 0.2 wt. % to 2.1 ± 0.3 wt. %. An accessory pyrochlore-structured phase with prototypical composition $Ca_2Ti_2O_6$ (JCPDS No. 04-0103, space group *Fd-3m*) was formed, with an intense reflection at $2\theta = 31.1°$ [34]. It was not possible to resolve the $Ca_2Ti_2O_6$ by SEM, presumably due similar backscattered electron coefficient to the accompanying perovskite and/or zirconolite-2M phase, yet the phase comprised 10.9 ± 0.5 wt. %. It is likely that partial incorporation of Ce occurred within both $CaTiO_3$ and $Ca_2Ti_2O_6$ phases, producing similar BSE contrast. Our previous attempts to form $CaZrTi_2O_7$ by RSPS resulted in approximately 2.1 wt. % $CaTiO_3$, with partial Ti^{3+} speciation confirmed by paramagnetic electron resonance measurements [13]. Furthermore, in the case of Clark et al., a sample of $CaZr_{0.5}Ce_{0.5}Ti_2O_7$ was sintered in air, and subsequently consolidated by SPS [22]. During this process, a perovskite fraction with stoichiometry $Ca_{0.40}Ce_{0.40}TiO_3$

Table 2
Comparison between nominal and calculated zirconolite-2M composition derived from quantitative EDS data, normalised to seven oxygen atoms. Errors are quoted in parentheses to 1 s.d.

Degree of Substitution	Nominal Composition	Observed Composition from EDS	Archimedes Density (g/cm^3)	Theoretical Density (g/cm^3)
x = 0.05	$Ca_{0.95}Ce_{0.05}ZrTi_{1.90}Cr_{0.10}O_7$	$Ca_{1.01(7)}Ce_{0.03(1)}Zr_{0.88(9)}Ti_{2.00(5)}Cr_{0.08(1)}O_7$	3.991 ± 0.032	4.528 ± 0.0001
x = 0.10	$Ca_{0.90}Ce_{0.10}ZrTi_{1.80}Cr_{0.20}O_7$	$Ca_{0.96(4)}Ce_{0.07(1)}Zr_{0.89(5)}Ti_{1.90(4)}Cr_{0.17(3)}O_7$	3.949 ± 0.083	4.598 ± 0.0002
x = 0.15	$Ca_{0.85}Ce_{0.15}ZrTi_{1.70}Cr_{0.30}O_7$	$Ca_{0.89(6)}Ce_{0.12(1)}Zr_{0.94(9)}Ti_{1.79(5)}Cr_{0.26(1)}O_7$	4.071 ± 0.071	4.674 ± 0.0002
x = 0.20	$Ca_{0.80}Ce_{0.20}ZrTi_{1.60}Cr_{0.40}O_7$	$Ca_{0.88(6)}Ce_{0.15(2)}Zr_{0.97(9)}Ti_{1.70(8)}Cr_{0.29(4)}O_7$	4.045 ± 0.035	4.734 ± 0.0002
x = 0.25	$Ca_{0.75}Ce_{0.25}ZrTi_{1.50}Cr_{0.50}O_7$	$Ca_{0.82(5)}Ce_{0.21(2)}Zr_{0.92(8)}Ti_{1.67(7)}Cr_{0.39(4)}O_7$	3.881 ± 0.055	4.790 ± 0.0002
x = 0.30	$Ca_{0.70}Ce_{0.30}ZrTi_{1.40}Cr_{0.60}O_7$	$Ca_{0.77(7)}Ce_{0.25(3)}Zr_{0.99(13)}Ti_{1.56(8)}Cr_{0.44(4)}O_7$	3.874 ± 0.040	4.855 ± 0.0002
x = 0.35	$Ca_{0.65}Ce_{0.35}ZrTi_{1.30}Cr_{0.70}O_7$	$Ca_{0.68(7)}Ce_{0.30(4)}Zr_{1.01(10)}Ti_{1.46(8)}Cr_{0.52(6)}O_7$	3.895 ± 0.032	4.915 ± 0.0002

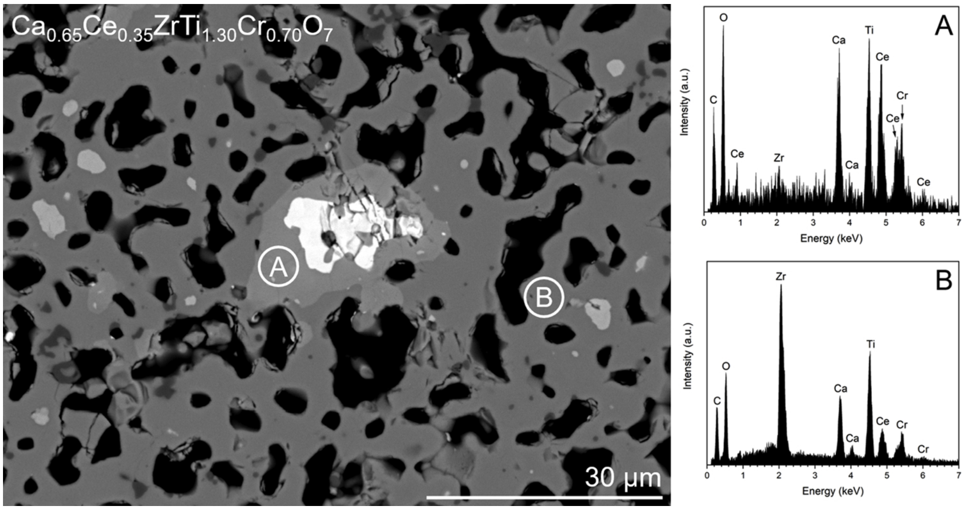

Fig. 6. EDS spot analysis of A) Ce-bearing perovskite; B) zirconolite-2M.

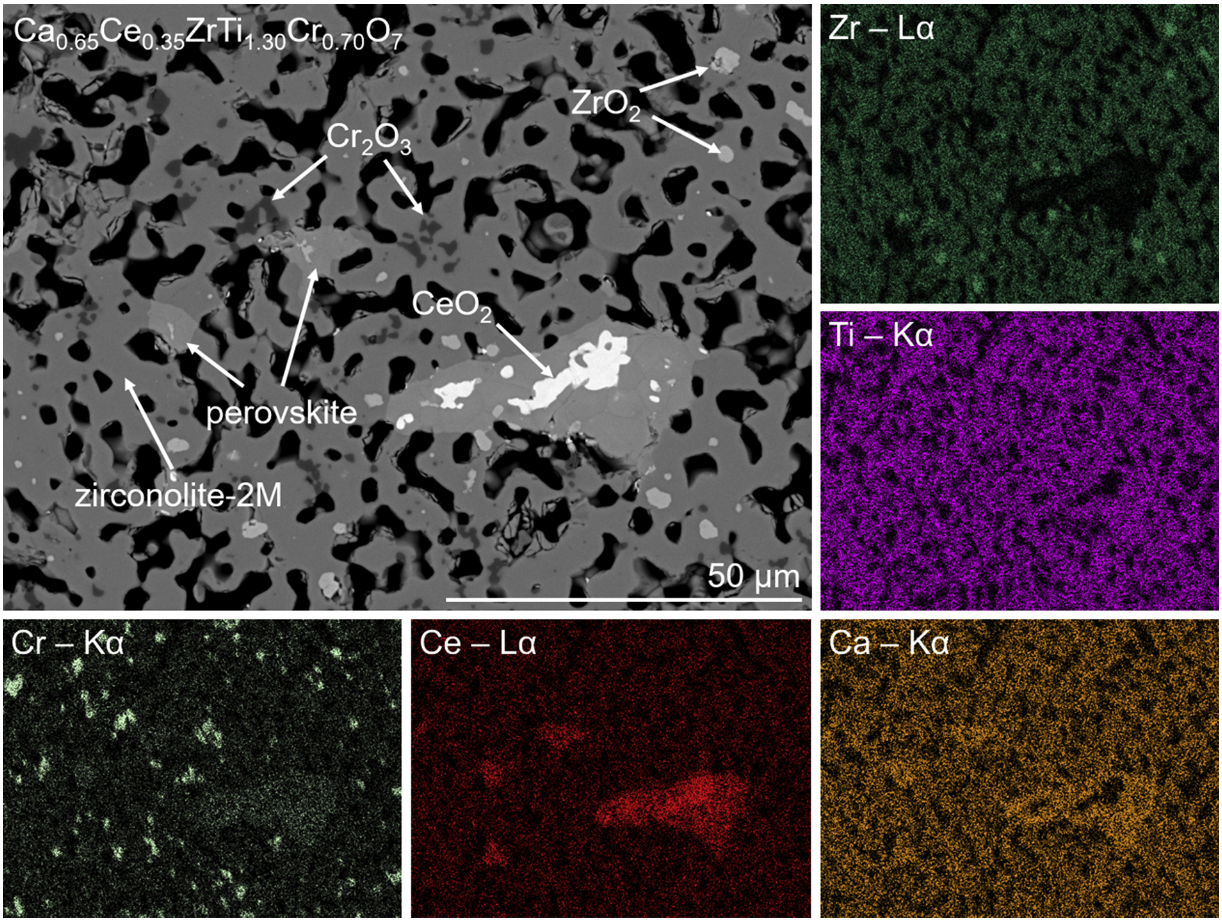

Fig. 7. Representative backscattered electron micrograph and corresponding elemental distribution for specimen with nominal composition x = 0.35. Black regions are porosity. (For interpretation of the references to colour in this figure legend, the reader is referred to the web version of this article).

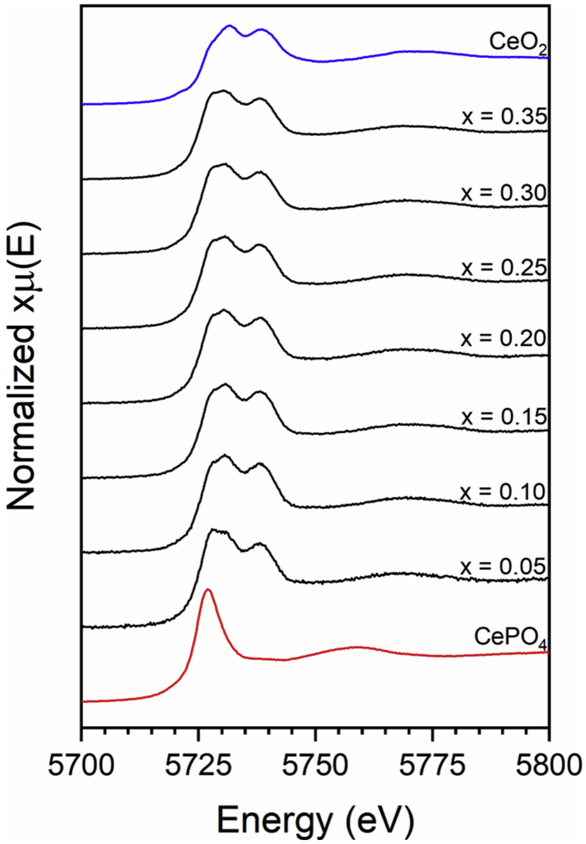

Fig. 8. XANES spectra at the Ce L_3-edge for compositions in the range $Ca_{1-x}Ce_xZrTi_{2-2x}Cr_{2x}O_7$ ($0.05 \le x \le 0.35$), in comparison to Ce^{4+} and Ce^{3+} standards (CeO_2 and $CePO_4$ respectively).

Table 3
Linear combination fitting of Ce L_3 XANES data relative to CeO_2 and $CePO_4$ standards.

Composition	Cerium Speciation (%)		R-factor
	Ce^{3+}	Ce^{4+}	
$Ca_{0.95}Ce_{0.05}ZrTi_{1.90}Cr_{0.10}O_7$	27.3 ± 1.1	72.7 ± 1.5	0.0119
$Ca_{0.90}Ce_{0.10}ZrTi_{1.80}Cr_{0.20}O_7$	15.7 ± 1.0	84.3 ± 1.5	0.0108
$Ca_{0.85}Ce_{0.15}ZrTi_{1.70}Cr_{0.30}O_7$	14.9 ± 0.9	85.1 ± 1.4	0.0073
$Ca_{0.80}Ce_{0.20}ZrTi_{1.60}Cr_{0.40}O_7$	16.4 ± 1.1	83.6 ± 1.5	0.0108
$Ca_{0.75}Ce_{0.25}ZrTi_{1.50}Cr_{0.50}O_7$	18.7 ± 1.0	81.3 ± 1.5	0.0096
$Ca_{0.70}Ce_{0.30}ZrTi_{1.40}Cr_{0.60}O_7$	20.4 ± 0.9	79.6 ± 1.4	0.0075
$Ca_{0.65}Ce_{0.35}ZrTi_{1.30}Cr_{0.70}O_7$	21.9 ± 0.8	78.1 ± 1.4	0.0079

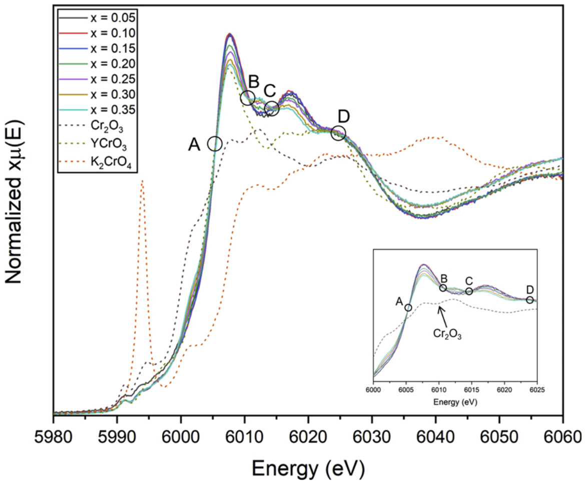

Fig. 9. Cr K XANES in the range 5980 – 6060 eV with Cr_2O_3, $YCrO_3$ and K_2CrO_4 reference compounds.

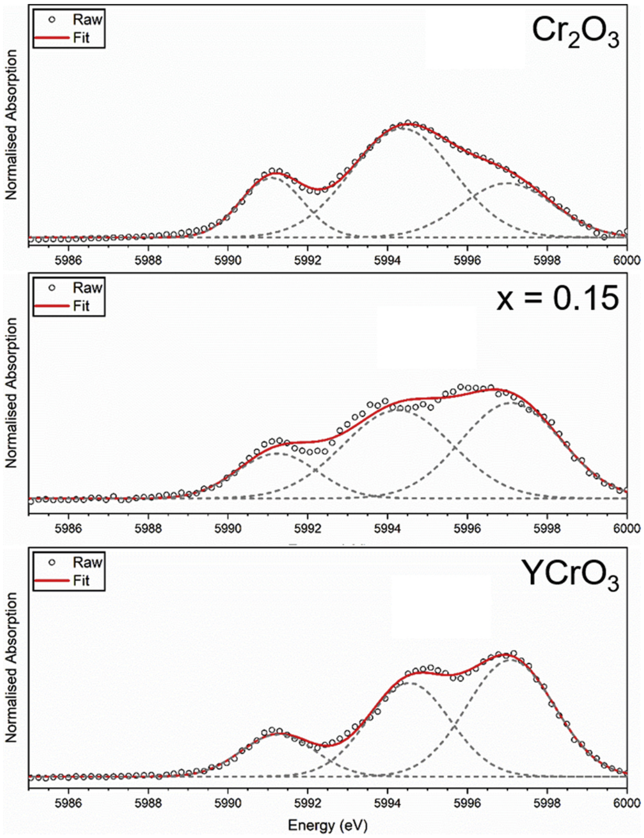

Fig. 10. Deconvolution of Cr K pre-edge region for Cr_2O_3, 'x = 0.15', and $YCrO_3$.

was stabilised due to the reducing conditions imposed by the SPS graphite die, with 90 % reduction to the Ce^{3+} species determined by XANES. Therefore, it was understood that the SPS environment caused the partial reduction of Ce^{4+} to Ce^{3+} promoting the formation of a Ce-perovskite phase. XANES spectra for the sample corresponding to x = 0.20 processed by air sintering and RSPS, with respect to Ce^{3+} and Ce^{4+} reference compounds, are displayed in Fig. 13. The XANES features for the RSPS sample consisted of a single intense feature consistent with the Ce^{3+} reference compound. Linear combination analysis determined that a complete reduction to the Ce^{3+} species was achieved. In consideration of the reduction during SPS, the reduction of Ce^{4+} or Pu^{4+} and formation of undesirable perovskite phase may be suppressed by use of a boron nitride die [35], instead of graphite die used in this work. SEM-EDS analysis of the polished RSPS surface was in good agreement with XRD data, demonstrated in Fig. 14. A dense matrix of zirconolite-2M was observed, with multiple secondary phases distinguished by variation in backscattered electron contrast. These were confirmed by EDS analysis to be Cr_2O_3, ZrO_2 and (Ca,Ce)TiO_3. Ce incorporation in the perovskite phase (or $Ca_2Ti_2O_6$) was evidenced by backscattered electron contrast, as brighter grains indicated a high Ce-fraction.

4. Conclusions

The incorporation of Ce within $CaZrTi_2O_7$ zirconolite, with Cr acting as a charge compensation species, was investigated for the Ca_{1-}

$_xCe_xZrTi_{2-2x}Cr_{2x}O_7$ system. The densification achieved by a cold-press and sinter method was poor, and therefore this is not a practical choice of solid solution for Pu^{4+} immobilisation from the perspective of the ceramic microstructure, despite the efficacy of Cr as a charge compensator. High porosity was evidently overcome by the application of reactive spark plasma sintering, yet a significant disruption to the phase assemblage was observed, attributed to the total reduction of Ce to Ce^{3+} and subsequent increase in the Ce-perovskite phase fraction. Electron diffraction analyses were consistent with zirconolite adopting the 2M polytype at all levels of Ce incorporation for the CPS solid solution. Powder XRD and SEM analysis confirmed that zirconolite-2M was formed as a single phase for $0.00 \leq x \leq 0.15$. Cr^{3+} was fully incorporated within the zirconolite phase up to $x = 0.15$, after which phase separation occurred. Ce incorporation within the perovskite phase was observed for $x > 0.15$, yet even at maximum targeted wasteloading, the phase assemblage was comprised of ~ 94 wt. % zirconolite-2M. Ce L_3 XANES data and linear combination fitting with reference compounds confirmed ~ 80 % Ce^{4+}. It was concluded from Cr K-edge XANES data that Cr was incorporated into the zirconolite phase as Cr^{3+}. Deconvolution of the Cr K XANES pre-edge region for zirconolite produced features consistent with $YCrO_3$ reference compound, inferring octahedral coordination in the zirconolite phase as expected. The potential behaviour of a Pu bearing zirconolite ceramic charge balanced with Cr^{3+} could be hypothesised using this data. Pu can be present as trivalent and tetravalent cations, similar to Ce. It was inferred from Ce L_3 XANES that Ce was distributed mainly as Ce^{4+}. Accounting for discrepancies in redox behaviour, Pu is expected to be uniformly present as Pu^{4+}, as Ce has a greater propensity to undergo auto-reduction at high processing temperatures. At values for which $0.05 \leq x \leq 0.15$, Pu^{4+} could be expected to fully partition within zirconolite-2M. However, these data imply that a conventional sintering route using Cr as a charge compensating cation may produce a microstructure with elevated porosity. This paper also highlights an important caveat for the deployment of reactive spark plasma sintering for Pu-bearing zirconolites, demonstrating the need for careful compositional design and atmosphere selection to control redox reactions.

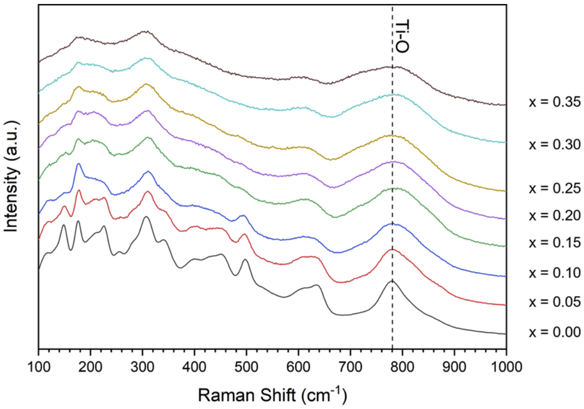

Fig. 11. Raman shift in the range 100 – 1000 cm^{-1} for $Ca_{1-x}Ce_xZrTi_{2-2x}Cr_{2x}O_7$ compositions.

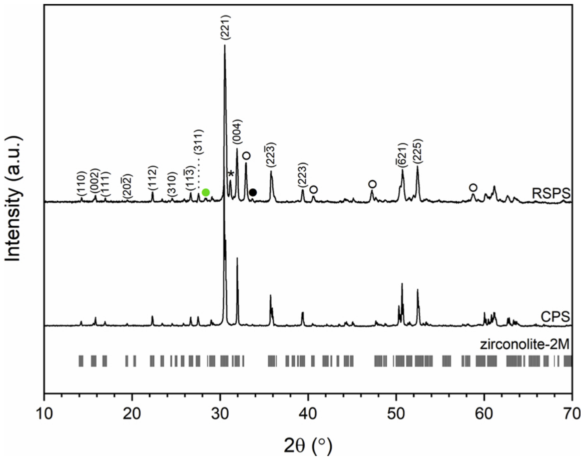

Fig. 12. Comparison of powder X-ray diffraction data of x = 0.20 composition synthesised by RSPS and CPS. $CaTiO_3$ reflections are labelled by open circles; ZrO_2 reflections are labelled by green filled circles; $Ca_2Ti_2O_6$ reflections are labelled by asterisk (*); Cr_2O_3 reflections are labelled by black filled circles. (For interpretation of the references to colour in this figure legend, the reader is referred to the web version of this article).

Declaration of Competing Interest

The authors declare that they have no known competing financial interests or personal relationships that could have appeared to influence the work reported in this paper.

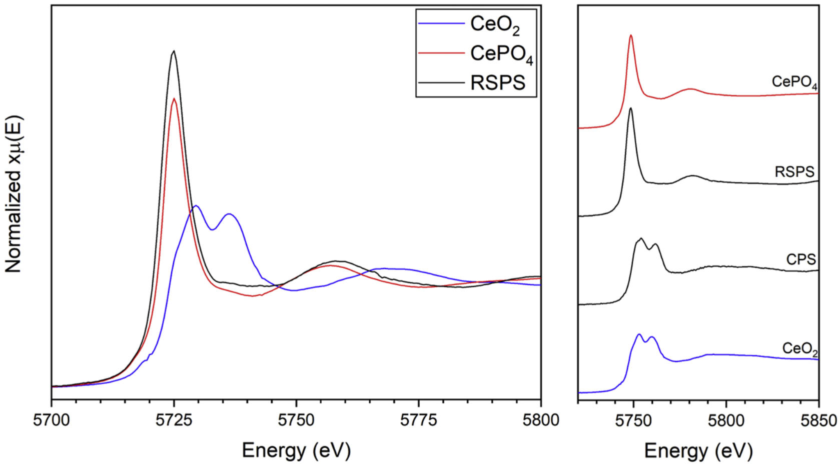

Fig. 13. Ce L_3 XANES data corresponding to $Ca_{0.80}Ce_{0.20}ZrTi_{1.60}Cr_{0.40}O_7$ processed by air sintering and RSPS, alongside CeO_2 and $CePO_4$ reference compounds.

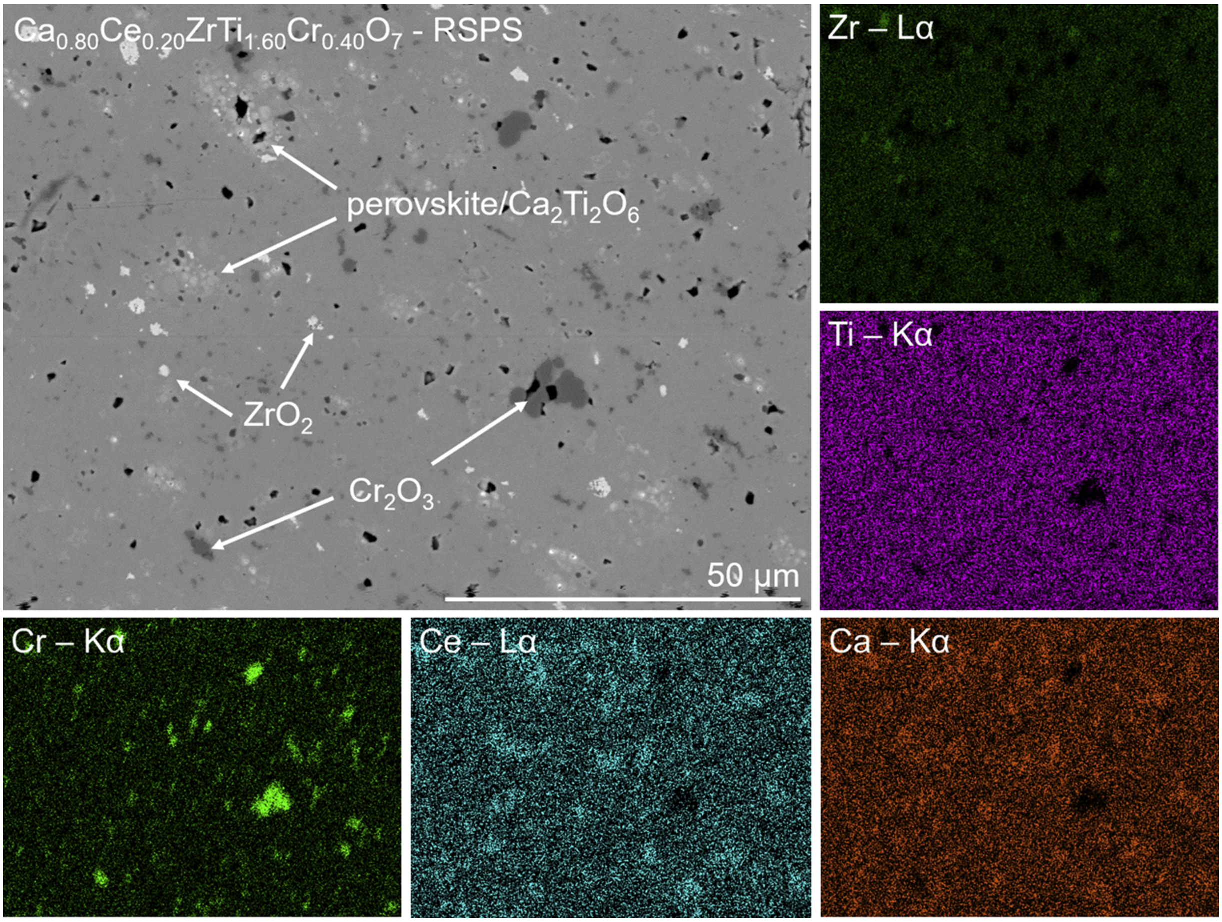

Fig. 14. Representative backscattered electron micrograph and corresponding elemental distribution for $Ca_{0.80}Ce_{0.20}ZrTi_{1.60}Cr_{0.40}O_7$ produced by RSPS.

Acknowledgements

LRB, NCH, SKS and LJG are grateful for financial support from the Nuclear Decommissioning Authority and EPSRC under grant numbersEP/M026566/1, EP/S01019X/1, EP/N017870/1 and EP/R511754/1. CLC and SML acknowledge EPSRC for funding under grant number EP/N017374/1. This research utilised the MIDAS/HADES facility at The University of Sheffield established with financial support from EPSRC and BEIS, under grant EP/T011424/1 [36]. We acknowledge Diamond Light Source for allocation of beam-time at Beamline B18 (Proposal SP24074-1). We acknowledge the Photon Factory Advisory Committee (Proposal No. 2019G586) for allocation of beam-time; the support of Yoshihiro Okamoto (Japan Atomic Energy Agency) and Noriko Usami (High Energy Accelerator Research Organization), during the experiment, is gratefully acknowledged.

References

[1] M.I. Ojovan, W.E. Lee, Introduction to Nuclear Waste Immobilisation, Elsevier Science Publishers, Amsterdam, Netherlands, 2005.

[2] N.C. Hyatt, Plutonium management policy in The United Kingdom: the need for a dual track strategy, Energy Policy 101 (2017) 303–309, https://doi.org/10.1016/j.enpol.2016.08.033.

[3] Nuclear Decommissioning Authority (UK), NDA plutonium Topic Strategy: Credible Options Technical Analysis, SAF/081208/006.2 (2009).

[4] K.P. Hart, Y. Zhang, E. Loi, Z. Aly, M.W.A. Stewart, A. Brownscombe, B.B. Ebbinghaus, W. Bourcier, Aqueous durability of titanate ceramics designed to immobilise excess plutonium, MRS Proc. 608 (1999) 353–358, https://doi.org/10.1557/proc-608-353.

[5] R.C. Ewing, Ceramic matrices for plutonium disposition, Prog. Nucl. Energy 49 (2007) 635–643, https://doi.org/10.1016/j.pnucene.2007.02.003.

[6] K.L. Smith, G.R. Lumpkin, M.G. Blackford, R.A. Day, K.P. Hart, The durability of synroc, J. Nucl. Mater. 190 (1992) 287–294, https://doi.org/10.1016/0022-3115(92)90092-y.

[7] R.C. Ewing, W.J. Weber, J. Lian, Nuclear waste disposal-pyrochlore ($A_2B_2O_7$): nuclear waste form for the immobilization of plutonium and 'minor' actinides, J. Appl. Phys. 95 (2004) 5949–5971, https://doi.org/10.1063/1.1707213.

[8] B.M. Gatehouse, I.E. Grey, R.J. Hill, H.J. Rossell, Zirconolite, $CaZr_xTi_{3-x}O_7$; Structure refinements for near-end-member compositions with x = 0.85 and 1.30, Acta Cryst. 37 (1981) 306–312, https://doi.org/10.1107/S0567740881002914.

[9] T.J. White, R.L. Segall, J.L. Hutchison, J.C. Barry, P.B. Hirsch, Polytypic behaviour of zirconolite, Proc. R. Soc. Lond. Ser. A 392 (1984) 343–358, https://doi.org/10.1098/rspa.1984.0035.

[10] A.A. Coelho, R.W. Cheary, K.L. Smith, Analysis and structural determination of Nd-substituted zirconolite-4M, J. Solid State Chem. 129 (1997) 346–359, https://doi.org/10.1006/jssc.1996.7263.

[11] M. Jafar, P. Sengupta, S.N. Achary, A.K. Tyagi, Phase evolution and microstructural studies in $CaZrTi_2O_7$-$Nd_2Ti_2O_7$ system, J. Am. Ceram. Soc. 97 (2014) 609–616, https://doi.org/10.1111/jace.12664.

[12] P.A. Bingham, R.J. Hand, M.C. Stennett, N.C. Hyatt, M.T. Harrison, The use of surrogates in waste immobilization studies: a case study of plutonium, MRS Proc. 1107 (2008) 421–428, https://doi.org/10.1557/proc-1107-421.

[13] S.-K. Sun, M.C. Stennett, C.L. Corkhill, N.C. Hyatt, Reactive spark plasma synthesis of $CaZrTi_2O_7$ zirconolite ceramics for plutonium disposition, J. Nucl. Mater. 500 (2018) 11–14, https://doi.org/10.1016/j.jnucmat.2017.12.021.

[14] A. Prasad, L. Malakkal, L. Bichler, J. Szpunar, Challenges in spark plasma sintering of cerium (IV) oxide, in: N.P. Bansal, R.H. Castro, M. Jenkins, A. Bandyopadhyay, S. Bose, A. Bhalla, J.P. Singh, M.M. Mahmoud, G. Pickrell, S. Johnson (Eds.), Processing, Properties, and Design of Advanced Ceramics and Composites II, John Wiley & Sons, Inc., New Jersey, 2018, pp. 217–224, , https://doi.org/10.1002/9781119423829.ch19.

[15] B.H. Toby, EXPGUI, a graphical user interface for GSAS, J. Appl. Crystallogr. 34 (2001) 210–213, https://doi.org/10.1107/S0021889801002242.

[16] J.A. Bearden, A.F. Burr, Reevaluation of X-ray atomic energy levels, Rev. Mod. Phys. 39 (1967) 125–142, https://doi.org/10.1103/revmodphys.39.125.

[17] H. Konishi, A. Yokoya, H. Shiwaku, H. Motohashi, T. Makita, Y. Kashihara, S. Hashimoto, T. Harami, T.A. Sasaki, H. Maeta, H. Ohno, H. Maezawa, S. Asaoka, N. Kanaya, K. Ito, N. Usami, K. Kobayashi, Synchrotron radiation beamline to study radioactive materials at the Photon Factory, Nucl. Instruments Methods Phys. Res. Sect. A 372 (1996) 322–332, https://doi.org/10.1016/0168-9002(95)01241-9.

[18] B. Ravel, M. Newville, ATHENA, ARTEMIS, HEPHAESTUS: data analysis for X-ray absorption spectroscopy using IFEFFIT, J. Synchrotron Radiat. 12 (2005) 537–541, https://doi.org/10.1107/S0909049505012719.

[19] M. Wilke, F. Farges, P.E. Petit, G.E. Brown, F. Martin, Oxidation state and coordination of Fe in minerals: an Fe K-XANES spectroscopic study, Am. Mineral. 86 (2001) 714–730, https://doi.org/10.2138/am-2001-5-612.

[20] K.R. Whittle, N.C. Hyatt, K.L. Smith, I. Margiolaki, F.J. Berry, K.S. Knight, G.R. Lumpkin, Combined neutron and X-ray diffraction determination of disorder in doped zirconolite-2M, Am. Mineral. 97 (2012) 291–298, https://doi.org/10.2138/am.2012.3848.

[21] E.R. Vance, G.R. Lumpkin, M.L. Carter, D.J. Cassidy, C.J. Ball, R.A. Day, B.D. Begg, Incorporation of uranium in zirconolite ($CaZrTi_2O_7$), J. Am. Ceram. Soc. 85 (2002) 1853–1859, https://doi.org/10.1111/j.1151-2916.2002.tb00364.x.

[22] B.M. Clark, S.K. Sundaram, S.T. Misture, Polymorphic transitions in cerium-substituted zirconolite ($CaZrTi_2O_7$), Sci. Rep. 7 (2017) 5920, https://doi.org/10.1038/s41598-017-06407-5.

[23] B.D. Begg, E.R. Vance, The incorporation of cerium in zirconolite, MRS Proc. 465 (1996) 333–340, https://doi.org/10.1557/proc-465-333.

[24] B.D. Begg, E.R. Vance, G.R. Lumpkin, Charge compensation and the incorporation of cerium in zirconolite and perovskite, MRS Proc. 506 (1997) 79–86, https://doi.org/10.1557/proc-506-79.

[25] B.D. Begg, E.R. Vance, S.D. Conradson, The incorporation of plutonium and neptunium in zirconolite and perovskite, J. Alloys Compd. 271–273 (1998) 221–226, https://doi.org/10.1016/S0925-8388(98)00058-9.

[26] N.C. Hyatt, R.R. Schwarz, P.A. Bingham, M.C. Stennett, C.L. Corkhill, P.G. Heath, R.J. Hand, M. James, A. Pearson, S. Morgan, Thermal treatment of simulant plutonium contaminated materials from the Sellafield site by vitrification in a blast-furnace slag, J. Nucl. Mater. 444 (2014) 186–199, https://doi.org/10.1016/j.jnucmat.2013.08.019.

[27] R.D. Shannon, Revised effective ionic radii and systematic studies of interatomie distances in halides and chaleogenides, Acta Cryst. 32 (1976) 751–767, https://doi.org/10.1107/s0567739476001551.

[28] S. Ould-Chikh, O. Proux, P. Afanasiev, L. Khrouz, M.N. Hedhili, D.H. Anjum, M. Harb, C. Geantet, J.-M. Basset, E. Puzenat, Photocatalysis with chromium-doped TiO_2: bulk and surface doping, ChemSusChem 7 (2014) 1361–1371, https://doi.org/10.1002/cssc.201300922.

[29] D. Cabaret, A. Bordage, A. Juhin, M. Arfaoui, E. Gaudry, First-principles calculations of X-ray absorption spectra at the K-edge of 3d transition metals: an electronic structure analysis of the pre-edge, Phys. Chem. Chem. Phys. 12 (2010) 5619–5633, https://doi.org/10.1039/b926499j.

[30] A. Salamat, P.F. McMillan, S. Firth, K. Woodhead, A.L. Hector, G. Garbarino, M.C. Stennett, N.C. Hyatt, Structural transformations and disordering in zirconolite ($CaZrTi_2O_7$) at high pressure, Inorg. Chem. 52 (2013) 1550–1558, https://doi.org/10.1021/ic302346g.

[31] R. Kaur, M. Gupta, P.K. Kulriya, S.S. Ghumman, Phase analysis and reduction behaviour of Ce dopant in zirconolite, J. Radioanal. Nucl. Chem. 322 (2019) 183–192, https://doi.org/10.1007/s10967-019-06536-3.

[32] M. Jafar, S.N. Achary, N.P. Salke, A.K. Sahu, R. Rao, A.K. Tyagi, X-ray diffraction and Raman spectroscopic investigations on $CaZrTi_2O_7$ - $Y_2Ti_2O_7$ system: delineation of phase fields consisting of potential ceramic host materials, J. Nucl. Mater. 475 (2016) 192–199, https://doi.org/10.1016/j.jnucmat.2016.04.016.

[33] B.M. Clark, P. Tumurugoti, S.K. Sundaram, J.W. Amoroso, J.C. Marra, K.S. Brinkman, Microstructures of melt-processed and spark plasma sintered ceramic waste forms, Metall. Mater. Trans. E 1 (2014) 341–348, https://doi.org/10.1007/s40553-014-0035-4.

[34] M. Sato, R. Tu, T. Goto, Preparation of pyrochlore $Ca_2Ti_2O_6$ by metal-organic chemical vapor deposition, Mater. Trans. 47 (2006) 2603–2605 https://www.jim.or.jp/journal/e/47/10/2603.html.

[35] O. Guillon, J. Gonzalez-Julian, B. Dargatz, T. Kessel, G. Schierning, J. Räthel, M. Herrmann, Field-assisted sintering technology/spark plasma sintering: mechanisms, materials, and technology developments, Adv. Eng. Mater. 16 (2014) 830–849, https://doi.org/10.1002/adem.201300409.

[36] N.C. Hyatt, C.L. Corkhill, M.C. Stennett, R.J. Hand, L.J. Gardner, C.L. Thorpe, The HADES facility for high activity decommissioning engineering & science: part of the UK national nuclear user facility, IOP Conf. Ser. Mater. Sci. Eng. 818 (2020) 012022, , https://doi.org/10.1088/1757-899x/818/1/012022.